High-power test of an interdigital *H*-mode drift tube linac for the J-PARC muon $g-2$ and electric dipole moment experiment

Y. Nakazawa,[1,*] E. Cicek,[2] K. Futatsukawa,[2] Y. Fuwa,[3] N. Hayashizaki,[4] T. Iijima,[5] H. Iinuma,[1] Y. Iwata,[6] Y. Kondo,[3,1] T. Mibe,[2] S. Mizobata,[2] T. Morishita,[3] M. Otani,[2] Y. Sue,[5] Y. Takeuchi,[7] and J. Tojo[7]

[1]*Graduate School of Science and Engineering, Ibaraki University, Mito, Ibaraki, 310-8512, Japan*
[2]*High Energy Accelerator Research Organization (KEK), Ibaraki, 305-0801, Japan*
[3]*Japan Atomic Energy Agency (JAEA), Tokai, Naka, Ibaraki, 319-1195, Japan*
[4]*Tokyo Institute of Technology, Tokyo, 152-8550, Japan*
[5]*Graduate School of Science, Nagoya University, Nagoya, 464-8602, Japan*
[6]*National Institute of Radiological Sciences, Chiba, 263-8555, Japan*
[7]*Kyushu University, Fukuoka, 819-0395, Japan*

(Received 1 August 2022; accepted 10 October 2022; published 7 November 2022)

We conducted a high-power test of a prototype cavity of a 324-MHz interdigital H-mode drift tube linac (IH-DTL) for the precise measurement of the muon anomalous magnetic moment ($g-2$) and electric dipole moment (EDM). This prototype cavity (short IH) was developed to verify the fabrication methodology for the IH-DTL cavity with a monolithic drift tube structure. The electromagnetic field distribution was measured and compared with the finite element method simulation results, and the fabrication accuracy of the monolithic drift tube was confirmed to satisfy the requirements. After 40 h of conditioning, the short IH was stably operated with an rf power of 88 kW, which corresponds to a 10% higher accelerating field than the design field (E_0) of 3.0 MV/m. In addition, the thermal characteristics and frequency response were measured, verifying that the experimental data were consistent with the three-dimensional model. In this paper, the design, fabrication, and low-power and high-power tests of this IH-DTL for muon acceleration are described.

DOI: 10.1103/PhysRevAccelBeams.25.110101

I. INTRODUCTION

Although the standard model (SM) has been used to successfully predict a wide variety of physics phenomena, the anomalous magnetic moment of muons (muon $g-2$), which is a sensitive probe of deficiencies in the SM, is significant. The Fermi National Accelerator Laboratory (FNAL-E989) measured muon $g-2$ with an accuracy of 0.46 ppm [1], which is consistent with a previous experiment, BNL-E821 [2], and these results showed a discrepancy of 4.2 standard deviations from the SM prediction [3]. These previous experiments have suffered from beam-derived uncertainties in their measurements because they used muons from a pion decay with a large emittance. We planned a new experiment (the E34 experiment [4]) to measure the muon $g-2$ and electric dipole moment (EDM) at the Japan Proton Accelerator Research Complex (J-PARC) with a completely independent approach from the previous experiments using low-emittance muon beams achieved by the original muon linear accelerator (linac). The E34 experiment aims to measure the muon $g-2$ with a precision of 0.1 ppm and search for the EDM with a sensitivity of approximately 10^{-21} e cm.

In the E34 experiment, thermal muonium production and laser dissociation produce ultraslow muons with a kinetic energy of 30 meV [5–7]. The generated ultraslow muons are electrostatically accelerated to 5.6 keV ($\beta(=v/c)=0.01$) and injected into the muon linac. The muon linac consists of a radio-frequency quadrupole linac (RFQ), an interdigital H-mode drift-tube linac (IH-DTL), disk and washer coupled cavity linacs (DAW-CCL), and disk-loaded accelerating structures (DLS) [8,9]. Muons are accelerated up to an energy of 212 MeV ($\beta=0.95$), avoiding significant emittance growth to satisfy the experimental requirement of a transverse divergence angle of less than 10^{-5}. As for the RFQ, the world's first rf acceleration of muons using a prototype RFQ for the J-PARC linac was demonstrated in 2017 [10,11].

The muons bunched and accelerated by the RFQ are accelerated from 0.34 to 4.3 MeV ($\beta=0.08$–0.28). The Alvarez DTL is widely used for this β region. However,

*20nd103s@vc.ibaraki.ac.jp

reducing construction costs is critical for the realization of our experiment. Therefore, we employed the alternating phase focusing (APF) [12] method. The APF method utilizes the transverse focusing force derived from the rf electric field by appropriately selecting each gap's positive and negative synchronous phases. With this scheme, the structure can be drastically simplified by omitting the complicated focusing element–containing drift tubes (DT). The accelerating efficiency is reduced due to the alternating synchronous phase, but it can be compensated for by using the H-mode structure, with which a higher transit time factor can be obtained using the π-mode acceleration. The APF is usually used for heavy ion linacs having relatively low beam currents [13–15]. For our muon linac, the beam current is very low, so we considered it applicable, although more careful treatment of the rf transverse force was necessary for the beam dynamics design [16] because of the much lighter mass of the muon. Table I shows the main parameters of the IH-DTL for the muon linac.

Moreover, for the APF IH-DTL cavity, a three-piece structure [17], which is also effective for cost reduction, can be applied. A center plate and two semicylindrical side shells made of oxygen-free copper (OFC) are bolted together to form the cavity structure. On the center plate, all DTs are monolithically machined. With this method, the time-consuming DT alignment procedure is not required. However, because this is the first time that the monolithic DT structure is being applied to a 324-MHz IH-DTL cavity for muon acceleration, it should be confirmed before fabricating the actual cavity that a field accuracy of less than $\pm 2\%$, which is required by the beam dynamics design [18], can be achieved only by machining.

Although the designed peak surface field of our IH-DTL cavity is relatively high (2.0 Kilpatrick limit [19]), it will be operated with a very low duty factor of 0.1%. Therefore, we decided not to apply any surface treatment for further cost reduction. Vacuum-tight movable slug tuners will be used for both low-power tuning and high-power operation. To simplify the structure of the movable tuner, rf contactors between the slug and cavity are omitted.

As the first step of the muon IH-DTL project, we developed a short-length IH-DTL (henceforth called "short IH") as a prototype. The main purpose of the short IH is to verify the above-mentioned technical decision, but it is also capable of actually accelerating muons.

This paper describes the detailed structure and the low- and high-power test results of the short IH for muon linac. After introducing the basic design of the short IH in Sec. II, the low-power measurement results are discussed in Sec. III. Then, in Sec. IV, in addition to the high-power test results of the short IH, the thermal characteristics are evaluated. Finally, these results are summarized in Sec. V.

TABLE I. Main parameters of the IH-DTL for the muon linac.

Beam species	μ^+
Beam intensity	1×10^6/s
Beam pulse width	10 ns
Repetition rate	25 Hz
rf pulse width	40 μs
Duty factor	0.1%
Resonant frequency	324 MHz
Injection energy	0.34 MeV
Extraction energy	4.26 MeV

II. DESIGN OF THE SHORT-IH

The short IH corresponds to the upstream one-third of the full-length IH-DTL (full IH), as shown in Fig. 1. The short IH has the same synchronous phase as the first 6 cells of the full IH, which has 16 cells, and it can accelerate muons from 0.34 to 1.30 MeV ($\beta = 0.08$–0.15).

The rf design of the short IH was conducted using CST MICROWAVE STUDIO (MWS) [20]. Figures 2 and 3 show its structure. The short IH has the same drift tube radius, cell length, and ridge width as the full IH. However, the end-cut depths of the ridge and cavity diameter were adjusted for the short IH to make the electric field distribution as flat as possible and tune the frequency. The fundamental resonant

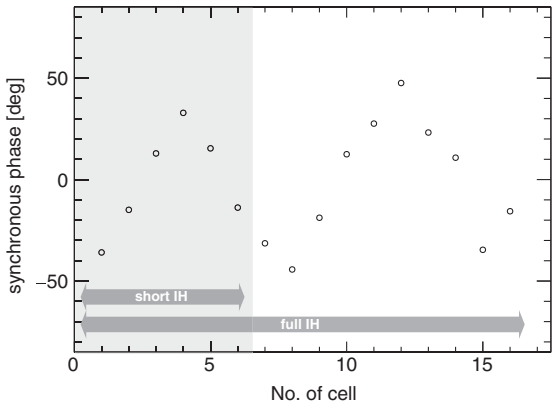

FIG. 1. Optimized phase array as a function of the cell number [16]. The short IH corresponds to the first six cells of the full IH.

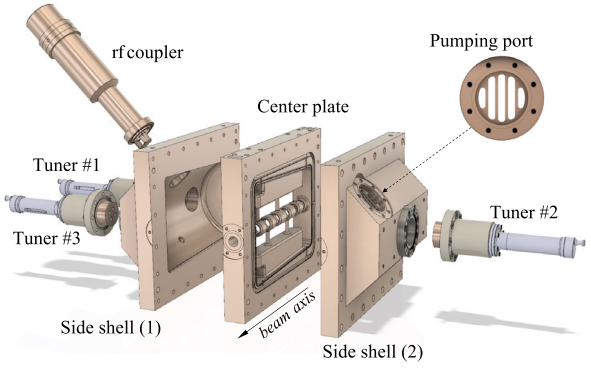

FIG. 2. Mechanical structure of the short IH.

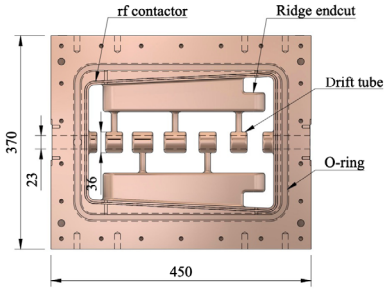

FIG. 3. Side view of the center plate.

frequency of the bare cavity was set to 321.88 MHz, which is slightly lower than the operating frequency for tunability. The unloaded quality (Q_0) value was calculated as 8600. Figure 4 shows the simulated results of the on-axis field distribution. Not only an accelerating electric field in the z-direction (E_z), but a magnetic field in the x-direction (H_x) and an electric field in the y-direction (E_y) are also significant due to the characteristics of the IH cavity. E_y is an asymmetric field along the axis, and the magnitude of E_y in each gap corresponds to 2%–12% of each E_z. The nominal accelerating field gradient (E_0) of the short IH is 3.0 MV/m on average and the nominal peak power calculated from the above Q_0 is 65 kW.

After creating the rf design, a beam dynamics simulation was conducted to confirm the beam quality at the short-IH exit. Figure 5 shows the phase-space distribution at the short-IH exit simulated with a general particle tracer (GPT) [21], and Table II summarizes the design and output beam parameters of the full IH and short IH. For this simulation, realistic input distribution from the particle simulation up to the RFQ exit [9,22] was used. The difference in horizontal and vertical rms emittance was derived from the difference in the distributions of the muon source [4]. The emittance growths in the horizontal and vertical directions from the RFQ exit were 5.7% and 3.0%, respectively. These are due

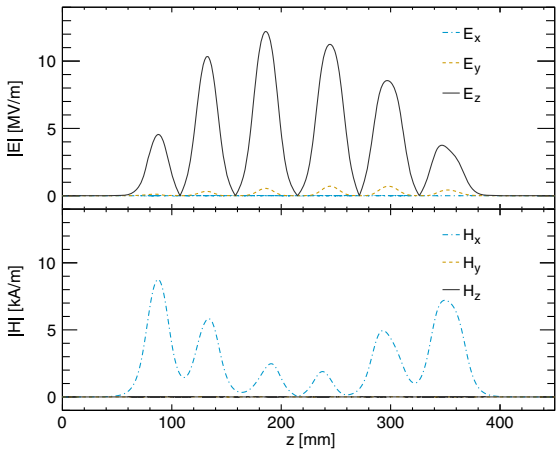

FIG. 4. Simulated on-axis EM fields of the short IH at the nominal voltage. The average accelerating field is 3.0 MV/m.

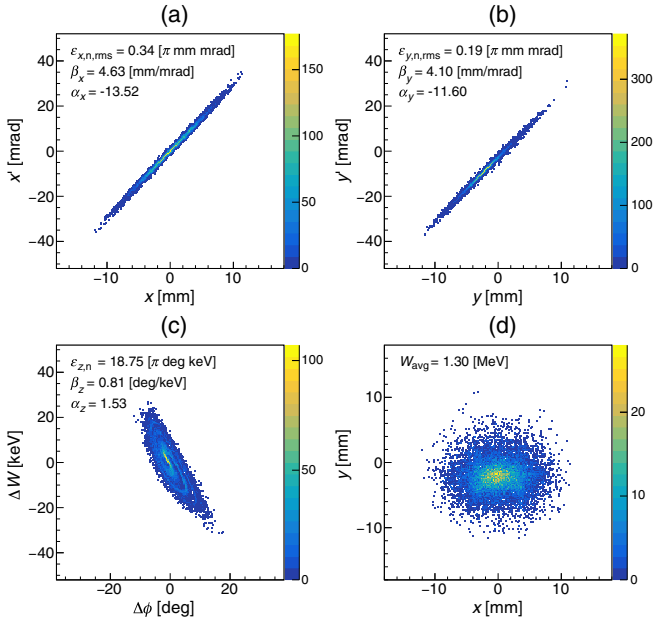

FIG. 5. Calculated phase-space distributions at the short-IH exit. (a) the horizontal divergence angle x' vs x, (b) the vertical divergence angle y' vs y, (c) energy spread $\Delta W(W - 1.3\ \mathrm{MeV})$ vs phase spread $\Delta\phi$, and (d) y vs x.

to the dipole field (E_y, H_x), as shown in Fig. 4. Without this effect, the transverse emittance growths are decreased by a few percent [16]. The total beam transmission, including the muon survival rate, of the short IH was 99.3%.

As described in the previous section, the three-piece structure was adopted. Two side shells and a center plate were bolted together, as shown in Fig. 2, and on the center plate, DTs were monolithically machined, as shown in Fig. 3. Each of them was made of OFC class 1. A coil spring rf contactor made of beryllium copper was installed

TABLE II. Comparison of the full IH and short IH.

Parameters	Full IH	Short IH
Number of the cells	16	6
Extraction energy (MeV)	4.26	1.30
Cavity length (m)	1.45	0.45
Averaged accelerating field (MV/m)	3.6	3.0
Maximum surface field (MV/m)	35.4 ($2.0\ E_k^a$)	34.7 ($1.9\ E_k^a$)
Nominal peak power (kW)	310[b]	65[b]
Horizontal emittance growth (%)	9.8	5.7
Vertical emittance growth (%)	7.9	3.0
Longitudinal emittance growth (%)	16.8	1.9
Transmission (%)	99.97	99.85
Transient time (ns)	25	13
Survival rate (%)	98.9	99.4
Total transmission (%)	98.9	99.3

[a]Kilpatrick limit.
[b]Calculated from a simulated Q_0 value.

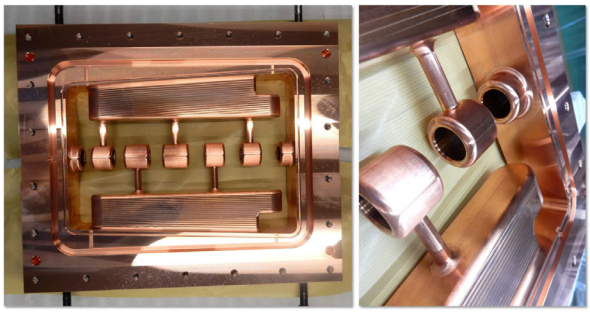

FIG. 6. Fabricated center plate of the short IH.

in the grooves on both sides of the center plate, and the vacuum was sealed with Viton O-rings.

Figure 6 shows the machined center plate of the short IH. After the machining, the cavity dimensions were measured with a three-dimensional coordinate measuring machine. The difference between the measured and designed values for the radius of the DT was less than 50 μm. The gap length between the DTs was accurately placed within the tolerance of 200 μm. After the machining, no surface treatments, such as baking, acid rinsing, chemical polishing, or chromate treatment, were applied to reduce the fabrication cost.

The short-IH cavity has three tuner ports, three rf pickup ports, one rf coupler port, and a pumping port with slits, as shown in Fig. 2. The cross-sectional view of the cavity is shown in Fig. 7. The three tuners are manually movable with a 50-mm stroke. These tuners are used not only for low-power tuning but also for high-power operation. To simplify the tuner structure, no rf contactors were used even under high-power operation. A loop-type rf coupler was used to supply the rf power [23]. The material of the conductor was also OFC, and the rf window was made of TiN-coated alumina ceramics (KYOCERA A479S [24]). An rf contactor was used for high-power operation, as shown in Fig. 7. The coupling coefficient of the coupler (β_{coupler}) can be fine-tuned by rotating the loop antenna. The size and default angle of the loop antenna were determined using a low-power coupler [25]. The β_{coupler}

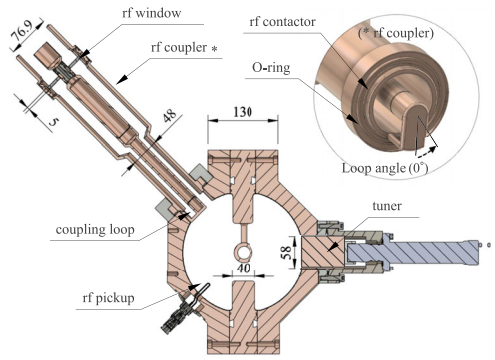

FIG. 7. Cross-sectional view of the short IH. The tuners have no rf contactors to simplify the structure.

was set to the critical coupling under high-power operation because the muon beam current is so small ($\sim 10^6$ muons/s with 25 bunches) that the beam loading is assumed to be negligible.

III. LOW-POWER MEASUREMENT

After the fabrication of the short IH, a series of low-power measurements was performed. First, the resonant frequency and Q_0 value of the cavity without tuners and rf coupler were measured using a vector network analyzer (VNA). The measured frequency and Q_0 values were 321.36 MHz and 7800, respectively. This Q_0 value corresponds to 91% of the simulated Q_0 value.

The tuners and coupler were then installed in the cavity. Then, the frequency was roughly adjusted to 324 MHz with the tuners, and the coupling coefficient of the coupler was adjusted to critical coupling by rotating the loop angle to approximately 50°, as shown in Fig 7. And the frequency was fine-tuned to be 324 MHz. Figure 8 shows the responses of the frequency and Q_0 value with respect to the tuner insertion lengths (L_{tuner}). Here, the origin of L_{tuner} is defined as the position of the surface on the outer cavity wall. The measured and simulated tuning frequencies for the three tuners were 3.24 MHz and 3.27 MHz, respectively, and they were found to be in good agreement. The measured Q_0 values were also consistent with the simulation results. The frequency was tuned to 324.00 MHz by adjusting the L_{tuner} of tuners #1, #2, and #3 to 45.2, 43.3, and 45.8 mm, respectively. After tuning the frequency, the β_{coupler} was measured as 1.01.

The results of the low-power tuning are summarized in Table III. The measured Q_0 value after the tuning was 7100, which corresponds to 86% of the simulated Q_0 value. The

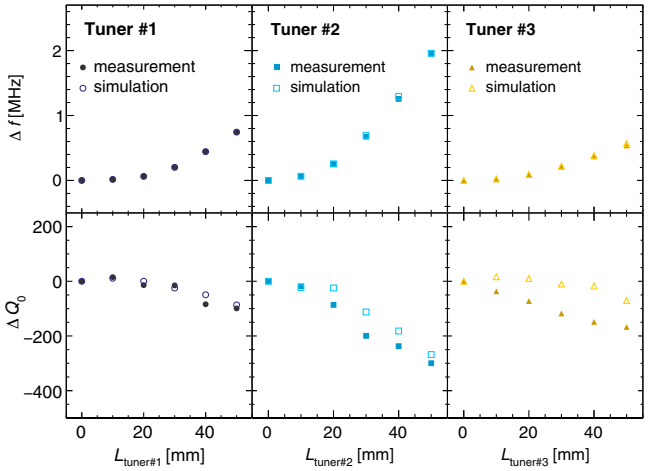

FIG. 8. Top: frequency shift as functions of the tuner insertion lengths of each tuner. The tunable ranges with the three tuners were 3.24 and 3.27 MHz in the measurement and simulation, respectively. (bottom) The unloaded Q (Q_0) shift dependence on L_{tuner}.

TABLE III. Result of the low-power tuning.

Parameters	Measurement	Simulation
(w/o tuners and coupler)		
Resonant frequency (MHz)	321.36	321.88
Q_0	7800	8600
(after tuning to 324.00 MHz)		
Q_0	7100	8300

degradation in Q_0 value due to the coil spring rf contactor between the center plate and the side shells, and the rf contactor-less tuners was within the acceptable levels. Considering the measured Q_0 value, the rf power required for the nominal voltage is 75 kW.

After low-power tuning, the electromagnetic field distribution of the cavity was measured using the bead-pull method [26]. A stepping motor pulled an aluminum spherical bead of 1.5-mm radius at a constant speed along the beam axis, and the frequency shift was measured continuously with a VNA.

Figure 9 shows the measured and simulated frequency shift along the beam axis. The simulated frequency shifts were calculated from $\propto \varepsilon_0 E^2 - \mu_0 H^2/2$, where $E(\text{or}\, H) = \sqrt{E(H)_x^2 + E(H)_y^2 + E(H)_z^2}$, ε_0 is the dielectric constant of vacuum, and μ_0 is the magnetic permeability of vacuum. The field error was evaluated by taking the difference between the square root of the measured and simulated frequency shifts. The difference in the field distribution of the gap region indicated by the gray dotted line was less than 2%. Here, the horizontal bar corresponds to the gap regions, and the field error indicates the average value within those regions. An error due to the bead's position in the y direction is less than 2%, and the measurement result

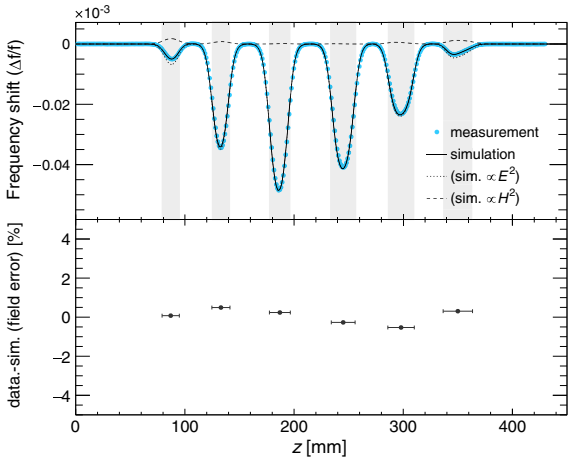

FIG. 9. Frequency shift distribution obtained with the bead pull measurement. Top: the measured and simulated frequency shift. The gray bands show the gap regions. Bottom: the difference between the measurement and the simulation (field error) in the gap region.

was within the uncertainty of measurement. These results reveal that the fabrication accuracy of the drift tube with a monolithic structure fulfills the requirement.

IV. HIGH-POWER TEST

In this section, the stability of the high-power operation of the cavity fabricated using the simplified process is described. Moreover, the thermal characteristics are compared with those observed during the simulation.

A. Experimental setup

The high-power test was conducted at the J-PARC linac building. The rf power from a 324-MHz klystron (Canon E3740A [27]) was applied to the cavity using waveguides (WR2300), coaxial lines, and the rf coupler. A photograph of the experimental setup is shown in Fig. 10. The coaxial line was reduced to WX77D from WX203D to match the rf coupler. The cavity was evacuated with a 240-L/s turbomolecular pump. The vacuum pressure in the cavity was measured using a Bayard–Alpert (BA) gauge, and an interlock was applied to turn off the rf power when the pressure exceeded 1.0×10^{-3} Pa. Three thermocouples were attached to the outer wall of the cavity to measure the cavity temperature, and one thermocouple was placed 2 m away from the cavity to measure the ambient temperature.

Figure 11 shows a block diagram of the high-power test system. A directional coupler was inserted between the coaxial line and the coupler to measure the rf power forwarded to and reflected from the cavity using power meters (SPANAWAVE 8542C [28]). The cavity pickup signal was also measured with the power meter. The data from the power meters were directly recorded by an input/output controller (IOC) of an experimental physics and industrial control system (EPICS). In addition, the input and output power of the directional coupler and cavity pickup were monitored using voltage standing wave ratio (VSWR) meters [29] and recorded through a

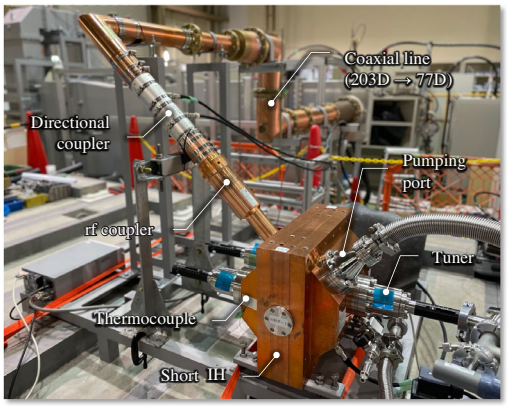

FIG. 10. Photograph of the experimental apparatus of the high-power test of the short IH.

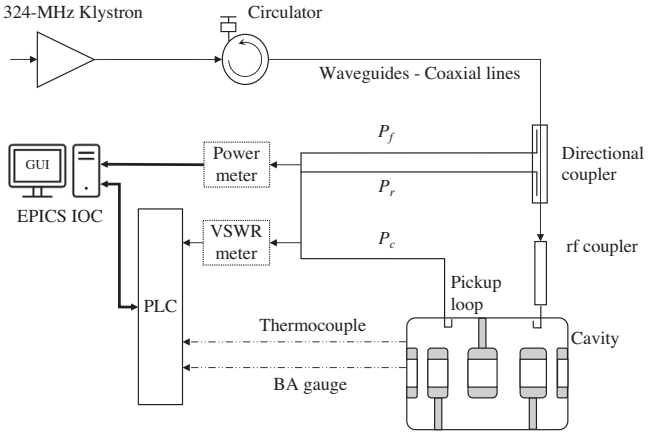

FIG. 11. Block diagram of the high-power test system. The interlock is triggered by rf powers and vacuum levels.

programmable logic controller (PLC) system. The rf power was turned off by the reflection and VSWR values to protect the cavity and rf window of the coupler from excessive power.

B. Conditioning

Figure 12 shows the conditioning history. The high-power test was operated only during the daytime, and the horizontal axis of the plot shows the integrated rf on time. The vacuum pressure in the cavity was 2×10^{-4} Pa without the rf input power and 5–7 $\times 10^{-4}$ Pa with the rf input power. As described in Sec. I, no surface treatment process was applied to suppress the initial outgassing. As a result, a considerable amount of gas emissions and discharges occurred at the beginning of the conditioning. Therefore, the conditioning was started with a low duty factor (repetition rate of 1 Hz and pulse width of 20 μs), and the power was gradually ramped up. As conditioning progressed, the outgases steadily decreased. After 21 h, because the cavity trips and outgases were reduced, the duty factor was increased. It took 32 h from the start of the conditioning to achieve a nominal duty factor of 0.1% (25 Hz, 40 μs) and peak power of 75 kW, considering the measured Q_0 value, as described in Sec. III.

Figure 13 shows the rf waveforms of the forward, reflected, and cavity pickup voltages at the nominal peak power and duty factor. As described in Sec. III, the coupling coefficient of the coupler was set as critical, so the reflection was quite small.

After the optimum nominal power and duty factor were reached, holding tests with nominal and increased peak electric fields were conducted. The cavity trip occurred only twice during the 7-h holding test with nominal power. During the 7-h operation with 88 kW, which corresponded to a 10% increased voltage, there was no trip. These results reveal that, even though no surface treatment was applied and rf contactor-less movable tuners were used, the short IH can be operated quite stably if an appropriate conditioning process is followed. Note that, during the high-power operation, the frequency was manually adjusted to follow the frequency shift due to the thermal deformation of the cavity; this is described in the next subsection.

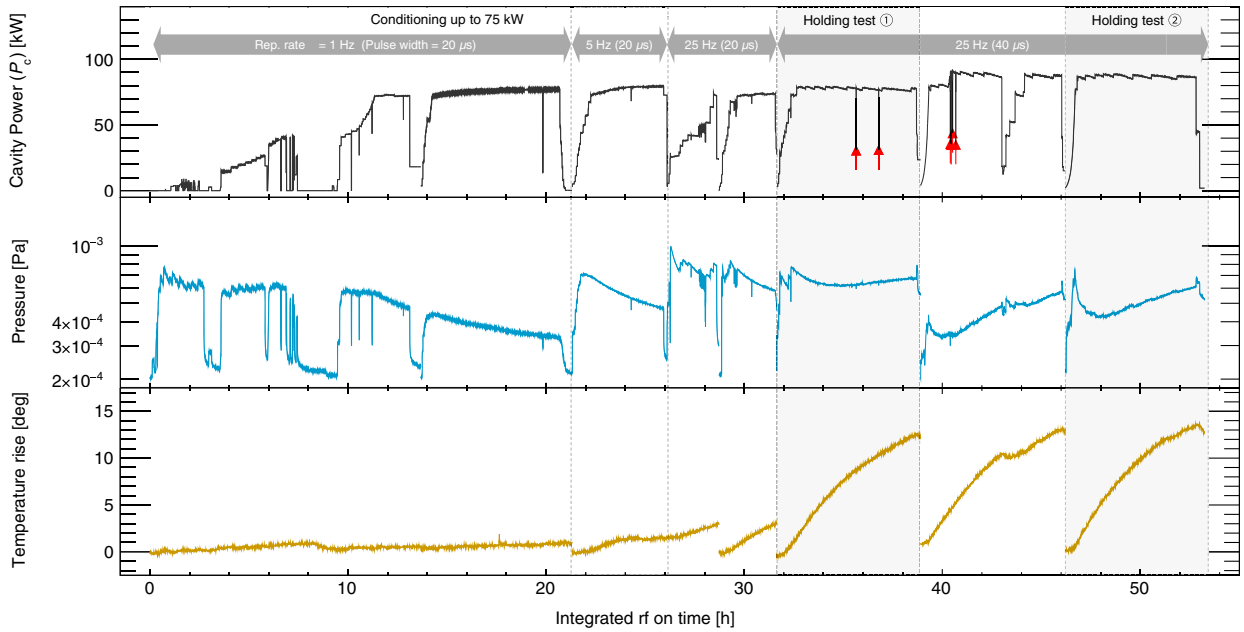

FIG. 12. Conditioning history of the short IH. The red arrows in the top plot indicate the cavity trip caused at the nominal duty factor. The temperature data show the difference between the average of the three thermocouples and the ambient temperature. The surface temperature of the cavity was measured at three different locations and showed no dependence on location.

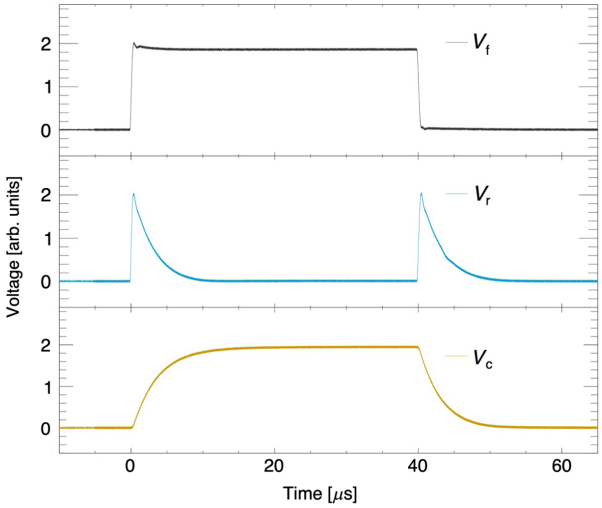

FIG. 13. rf waveforms of forward (top), reflected (middle), and cavity pickup voltages (bottom) at the nominal peak power of 75 kW.

C. Thermal characteristics

The thermal characteristics of the short IH were measured and compared with the results of a three-dimensional finite element method (FEM) analysis. Because the short IH has no water-cooling structure, the temperature rise was significant, and conversely, it was suitable for the verification of the FEM model. Although the outer cavity wall of the full IH will be water cooled, it is difficult to cool the monolithic DT directly. Therefore, thermal analysis is still essential in designing the full IH.

The temperature distribution and deformation of the short IH due to the power dissipation were analyzed using CST MPHYSICS STUDIO (MPS). To simplify the calculation, detailed structures of components such as slug tuners and rf contactors are omitted in this analysis. First, the power dissipation distribution of the cavity surface was calculated using CST MWS , as shown in Fig. 14, and input into MPS. The steady-state temperature distribution in the cavity was

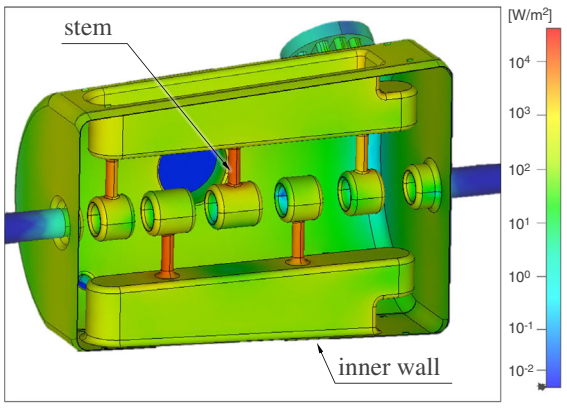

FIG. 14. Simulated power dissipation distribution on the cavity surface with the peak power of 88 kW and nominal duty factor.

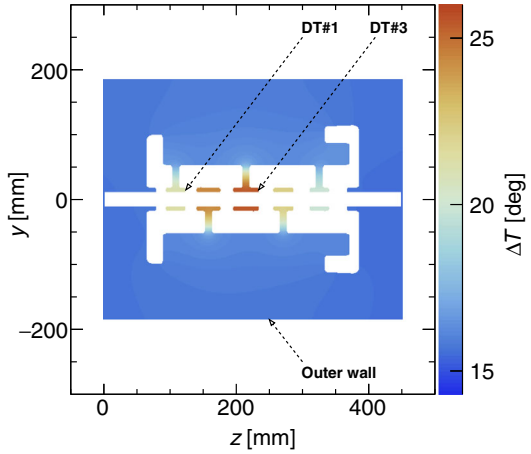

FIG. 15. Steady-state temperature distribution of the short IH with the peak power of 88 kW and a nominal duty factor. The distribution shows the temperature difference from the initial state of a uniform 24°C.

then derived, as shown in Fig. 15. Here, the heat transfer coefficient at the surface of the cavity outer wall was set to 8 W/m^2 K assuming natural convection to the atmosphere [30]. Furthermore, a duty factor of 0.1% was multiplied by the power dissipation input into the CST MPS. Heat dissipation was most significant at the stems, and because no cooling was applied to the DTs, the highest temperature rise occurred at the DT. Using the temperature distribution,

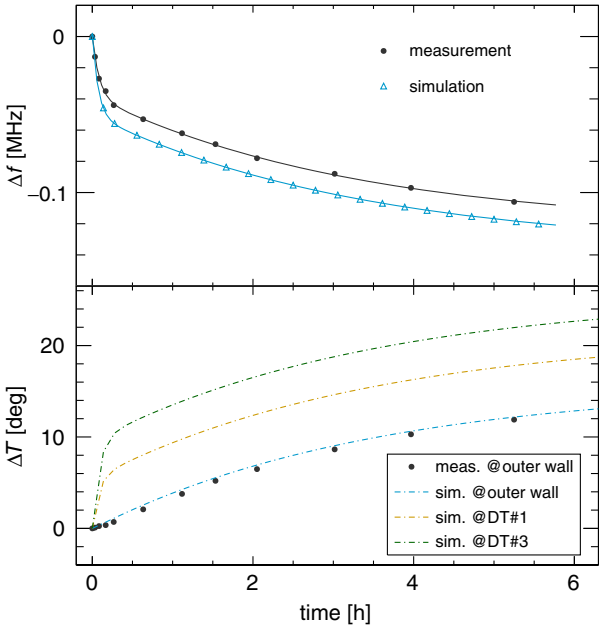

FIG. 16. Top: frequency shifts as functions of time after the rf power of 88 kW was turned on. The solid lines show the fitting results. Bottom: temperature drifts as functions of time. The data were plotted with the difference between ambient and cavity surface temperatures. The DT's temperature was increased rapidly within 0.3 h in the simulation.

TABLE IV. Fitting results for the measured and simulated transient response for frequency.

	a_1 (MHz)	a_2 (MHz)	τ_1 (h)	a_3 (MHz)	τ_2 (h)
Measurement	−0.12	0.038	0.086	0.084	3.31
Simulation	−0.14	0.051	0.074	0.086	3.37

the deformation from the initial state of uniform 24°C was calculated using CST MPS. These deformations were again input into the CST MWS, and the frequency shift was calculated. Moreover, the transient behavior of the temperature distribution was also analyzed, and the transient response of the frequency was evaluated using the same procedure as described above.

Figure 16 shows the measured and simulated transient behavior for an rf power of 88 kW. The horizontal axis represents the time after the rf power is turned on. The top figure represents the frequency shift (Δf) from 324 MHz. The measured and simulated data were fitted using

$$\Delta f = a_1 + a_2 \exp\left(\frac{t}{-\tau_1}\right) + a_3 \exp\left(\frac{t}{-\tau_2}\right). \quad (1)$$

The fitting parameters are summarized in Table IV. The measured parameters for the frequency term were consistent with the simulation results within several tens of kHz. The two measured time constants were also consistent with the simulation results.

The bottom figure in Fig. 16 represents the temperature drift of the cavity. The temperatures of the three thermocouples attached to the outer wall of the cavity were averaged, and their differences from the ambient temperature were plotted. The dotted lines show the simulated temperatures of the first and third drift tubes and outer cavity wall. The measured temperature of the outer cavity wall was in good agreement with the simulation result. In the simulation, the temperatures of the DTs increase with quicker time constants than the temperature of the outer wall during $t = 0.3$ h because the heat capacities of the DTs are smaller than that of the cavity wall. This result indicates that τ_1 and τ_2 are derived from the DT's local deformation and the entire cavity's thermal expansion, respectively. These results prove the validity of the simulations of the IH-DTL.

V. CONCLUSION

A high-power test of an IH-DTL (short IH) implementing the APF method for the J-PARC muon $g-2$/EDM experiment was successfully conducted. This short IH was developed to demonstrate the feasibility of the performance required for the full IH.

The machining accuracy of the 324-MHz IH-DTL with a monolithic structure was confirmed to satisfy the requirement, and the Q_0 degradation due to the rf contact-less tuners, which were applied for cost reduction, was within the acceptable levels.

After 40 h of conditioning, the peak power reached 88 kW, corresponding to a 10% higher accelerating field than the design field of 3.0 MV/m. Moreover, there was no trip during the 7-h operation at 88 kW. We demonstrated that even though no surface treatment was applied, the short IH could be operated very stably. Furthermore, the transient behavior of temperatures of the cavity surface and resonance frequency responses were measured and compared with those obtained the 3D FEM model. The measured frequency shift was consistent with that observed in simulations to within several tens of kHz.

These results confirm that the APF IH-DTL is practical as a cost-effective high-power rf cavity for muon acceleration with the capability of stable operation. This study proves that the design and fabrication methodology established by the short IH can be applied to the full IH required for the realization of the new muon $g-2$/EDM experiment.

ACKNOWLEDGMENTS

This work was supported by JSPS KAKENHI grant numbers JP15H03666, JP18H03707, JP16H03987, JP16J07784, JP20J21440, JP20H05625, JP21K18630, JP21H05088, JP22H00141; the JST FOREST Program (Grant No. JPMJFR212O); and the Natural Science Grant of the Mitsubishi Foundation (Grant No. 202111003). This paper is based on results obtained from a project commissioned by the New Energy and Industrial Technology Development Organization (NEDO) (Grant No. JPNP21502029-0). We express our appreciation to TIME Co., Ltd., who fabricated the short IH.

[1] B. Abi *et al.* (Muon g-2 Collaboration), Measurement of the Positive Muon Anomalous Magnetic Moment to 0.46 ppm, Phys. Rev. Lett. **126**, 141801 (2021).

[2] G. W. Bennett *et al.* (Muon $g-2$ Collaboration), Final report of the e821 muon anomalous magnetic moment measurement at BNL, Phys. Rev. D **73**, 072003 (2006).

[3] T. Aoyama *et al.*, The anomalous magnetic moment of the muon in the standard model, Phys. Rep. **887**, 1 (2020), the anomalous magnetic moment of the muon in the Standard Model.

[4] M. Abe *et al.*, A new approach for measuring the muon anomalous magnetic moment and electric dipole moment, Prog. Theor. Exp. Phys. **2019**, 053C02 (2019).

[5] P. Bakule *et al.*, Measurement of muonium emission from silica aerogel, Prog. Theor. Exp. Phys. **2013**, 103C01 (2013).

[6] G. A. Beer *et al.*, Enhancement of muonium emission rate from silica aerogel with a laser-ablated surface, Prog. Theor. Exp. Phys. **2014**, 091C01 (2014).

[7] J. Beare *et al.*, Study of muonium emission from laser-ablated silica aerogel, Prog. Theor. Exp. Phys. **2020**, 123C01 (2020).

[8] Y. Kondo *et al.*, Re-acceleration of ultra cold muon in J-PARC muon facility, in *Proceedings of 9th International Particle Accelerator Conference, IPAC'18, Vancouver, BC, Canada* (JACoW, Geneva, Switzerland, 2018), p. 5041.

[9] M. Otani, First muon acceleration and muon linear accelerator for measuring the muon anomalous magnetic moment and electric dipole moment, Prog. Theor. Exp. Phys. **2022**, 052C01 (2022).

[10] S. Bae *et al.*, First muon acceleration using a radio-frequency accelerator, Phys. Rev. Accel. Beams **21**, 050101 (2018).

[11] Y. Sue *et al.*, Development of a bunch-width monitor for low-intensity muon beam below a few MeV, Phys. Rev. Accel. Beams **23**, 022804 (2020).

[12] S. Minaev and U. Ratzinger, in *Proceedings of the 18th Particle Accelerator Conference, New York, 1999* (IEEE, New York, 1999).

[13] Y. Iwata, S. Yamada, T. Murakami, T. Fujimoto, T. Fujisawa, H. Ogawa, N. Miyahara, K. Yamamoto, S. Hojo, Y. Sakamoto, M. Muramatsu, T. Takeuchi, T. Mitsumoto, H. Tsutsui, T. Watanabe, and T. Ueda, Alternating-phase-focused IH-DTL for an injector of heavy-ion medical accelerators, Nucl. Instrum. Methods Phys. Res., Sect. A **569**, 685 (2006).

[14] Y. Iwata, S. Yamada, T. Murakami, T. Fujimoto, T. Fujisawa, H. Ogawa, N. Miyahara, K. Yamamoto, S. Hojo, Y. Sakamoto, M. Muramatsu, T. Takeuchi, T. Mitsumoto, H. Tsutsui, T. Watanabe, and T. Ueda, Performance of a compact injector for heavy-ion medical accelerators, Nucl. Instrum. Methods Phys. Res., Sect. A **572**, 1007 (2007).

[15] P. F. Ma, R. Tang, Y. Yang, S. X. Zheng, W. B. Ye, M. W. Wang, W. L. Liu, B. C. Wang, Q. Z. Xing, C. T. Du, H. Y. Zhang, J. Li, X. L. Guan, X. W. Wang, Z. M. Wang, and M. T. Qiu, Development of a compact 325 MHz proton interdigital *h*-mode drift tube linac with high shunt impedance, Phys. Rev. Accel. Beams **24**, 020101 (2021).

[16] M. Otani *et al.*, Interdigital *h*-mode drift-tube linac design with alternative phase focusing for muon linac, Phys. Rev. Accel. Beams **19**, 040101 (2016).

[17] The high-frequency cavity linear accelerators and buncher cavities, Japanese Patent No. 5692905 (P5692905), Time Incorporated Company, 2015.

[18] M. Otani *et al.*, Interdigital H-mode drift-tube linac design with alternative phase focusing for muon linac, in *Proceedings of the 13th Annual Meeting of Particle Accelerator Society of Japan, PASJ'16, Chiba, Japan* (2016), p. 858.

[19] W. D. Kilpatrick, Criterion for vacuum sparking designed to include both rf and dc, Rev. Sci. Instrum. **28**, 824 (1957).

[20] Computer Simulation Technology Studio Suite.

[21] General Particle Tracer, Pulsar Physics.

[22] M. Otani, N. Kawamura, T. Mibe, T. Yamazaki, K. Ishida, and G. Marshal, Simulation of surface muon beamline, UltraSlow muon production and extraction for the J-PARC $g-2$/EDM experiment, J. Phys. Conf. Ser. **1067**, 052018 (2018).

[23] Y. Nakazawa *et al.*, Multipacting simulations of coaxial coupler for IH-DTl prototype in muon accelerator, in *Proceedings of the 3rd J-PARC Symposium (J-PARC2019)*, https://journals.jps.jp/doi/pdf/10.7566/JPSCP.33.011128.

[24] KYOCERA, Characteristics of kyocera fine ceramics, https://global.kyocera.com/prdct/fc/product/pdf/material.pdf.

[25] Y. Nakazawa, H. Iinuma, Y. Iwata, Y. Iwashita, M. Otani, N. Kawamura, T. Mibe, T. Yamazaki, M. Yoshida, R. Kitamura, Y. Kondo, K. Hasegawa, T. Morishita, N. Saito, Y. Sue, N. Hayashizaki, and H. Yasuda, Development of inter-digital H-mode drift-tube linac prototype with alternative phase focusing for a muon linac in the J-PARC muon $g-2$/EDM experiment, J. Phys. Conf. Ser. **1350**, 012054 (2019).

[26] T. Wangler, *RF Linear Accelerators*, Physics Textbook (Wiley, New York, 2008).

[27] Canon, Canon-electron tubes and devices, e3740a, https://etd.canon/en/product/use/science/accel.html.

[28] Spanawave, Model 8542c dual input universal power meter, http://www.spanawave.com/store/Model-8542C-Dual-Input-Universal-Power-Meter.asp.

[29] R and k Company Limited, 4CH VSWR meter, https://rk-microwave.com/.

[30] P. Kosky, R. Balmer, W. Keat, and G. Wise, Mechanical engineering, in *Exploring Engineering*, 5th ed., edited by P. Kosky, R. Balmer, W. Keat, and G. Wise (Academic Press, New York, 2021), pp. 317–340, Chap. 14.